Chapter 5

Spin-glass state and exchange bias effect in $La_{1.5}Sm_{0.5}NiMnO_6$

5.1 Introduction

The intrinsic characteristic of the uncompensated moments across the phase boundaries controls the exchange bias (EB) considered as a fascinating topic in condensed matter research [48, 168–170]. The underlying competing FM and AFM interactions originate a SG state that shows local spin frustration and magnetic disorder offering exceptional phenomena of the EB and critical slowing dynamics [171–173]. For such materials, antisite disorder (ASD) induced competing exchange interactions and spin frustration are essential in stabilizing a magnetic inhomogeneous SG state [131, 174–176]. Investigating phase transition towards the SG phase remains a critical question of condensed matter [131, 174–176]. In the presence of external variants such as magnetic field and cooling/heating thermal cycles, SG phase exhibits behaviour of magnetization relaxation and memory effects [131, 168–176]. The degree of phase pinning boundaries across SG phase determines the mechanism of exchange bias effect [154, 171, 175–179]. The emergence of the SG phase has been manifested across the vast varieties of materials, such as diluted magnetic alloys [172–174], pyrochlores [176], garnet [177], perovskites [52, 178, 179], and magnetic heterostructures [168, 171, 180]. On the other hand, various numerical models have been proposed to describe the SG phase that found its implications in diverse fields ranging from neural networks to condensed matter [39, 131, 174].

Strongly correlated double perovskites (DP) manifest competing FM and AFM interactions mediated magnetic frustrated SG state and the underlying interplay between charge, lattice, orbital, and spin degrees of freedom [26, 50, 53, 61, 76, 103, 141, 142,

154, 181, 182]. Multiple studies have conducted to explore the role of ASD and antiphase boundaries (APB) of the underlying SG state to understand the microscopic mechanism of multi-functional properties in a family of materials that have shown tremendous abilities of controlled the functional and other magnetic properties [50, 141, 143, 183, 184]. For example, spin states and metal-insulator transition were reported in $La_{2-x}Sr_xNiMnO_6$ (x = 0, 0.2) [184].

The prominent presence of ASD promotes local frustration in these compounds. Moreover, the corner shared BO_6 and $B^{'}O_6$ octahedra distortion also contributes to the degree of frustration across APB that consists of pinned (frozen) spins [52, 141]. The modified sequencing of BO_6 and $B'O_6$ octahedra from their actual position by hosting B-O-B (B′ -O -B′) sites incorporating along with the intrinsic B -O -B′ couplings [183, 185]. These additional ASD modulate transport and magnetization properties of such inhomogeneous compounds [103, 183]. Through estimating the difference of experimentally observed saturation magnetization (M_s^o) from the calculated saturation magnetization (M_s^c) in the ordered phase, generally, ASD in such a system can be quantified [141]. Murthy *et al.* have observed coupling between FM and AFM interactions and ASD both reported for $La_{2-x}Sr_xCoMnO_6$ compound with A-site substitution [183].

For inhomogeneous magnetic frustrated system the interfacial anisotropy across FM and AFM phases induces EB effect that referred as a horizontal (vertical) deviation of the magnetic hysteresis loop drifted away from central position [168–171]. The experimental observations of EB effect across various frustrated compounds such as $Sm_{1.5}Ca_{0.5}CoMnO_6$ [50], $LaSrCoFeO_6$ [141], and La_2NiMnO_6 [77] have supported all these arguments. The LNMO is considered a model system for double perovskite materials that can also be designed by stacking the alternate $LaNiO_3$ and $LaMnO_3$ oxide materials as a super-lattice structure. Zhou *et al.* observed the evolution of SG phase and EB effect in $La_{0.7}Sr_{0.3}MnO_3/LaNiO_3$ bilayer [186]. Recent observations indicate that $SmNiO_3$ (SNO), which is a narrow band-gap semiconductor (MIT $\cong$ 400 K) can be converted as a Mott insulator with a band gap(E_g) of the order of 3 eV through site-substitution [187, 188]. The combined properties of $LaMnO_3/LaNiO_3$ super-lattice and renewed interest in $SmNiO_3$ have inspired us to investigate the functional properties of $La_{1.5}Sm_{0.5}NiMnO_6$ (LSNMO) compound. The sample was synthesized *sol-gel* route, already discussed. Herein, we report the ASD-driven magnetism and spin relaxation in the frustrated SG phase of the LSNMO compound. We found that the field-dependent isotherm loops display a robust EB effect that has been described using disordered pinning centers and frozen spin sites in this inhomogeneous system. Simultaneously, spin freezing dynamics, memory effect, and magnetic training effect in SG state. The spin-glass and exchange bias are corroborated

by memory & rejuvenation and training effect, respectively. This chapter highlights the presence of antisites via theoretical aspects and experimental (decrease in magnetization) approaches.

5.2 Computational details

All the calculations were performed using spin-polarised density functional theory (DFT) [189] as implemented in the plane-wave-based code Vienna AB-INITIO Simulation Package (VASP) [190] version 5.4. The kinetic energy cut off for the plane waves was taken as 400 eV throughout the calculations. The structure models were relaxed for ionic positions at fixed experimental lattice parameters until the Hellmann-Feynman forces on each atom were less than 10^{-2} eV/Å, and the convergence criterion was taken as 10^{-6} eV. We used the generalized gradient approximation (GGA) for the exchange-correlation (XC) functional in the form of Perdew-Burke-Ernzerhof (PBE) [191]. These materials do not have long-range dispersion; hence, the inclusion of any nonlocal correlation effect was discarded [192, 193]. Strongly correlated transition-metal oxides exhibit localized d-electrons with energy bands near the Fermi energy. Conventional local density approximations (LDA) or GGA within the DFT framework often fail to describe the electronic and magnetic properties accurately [194]. Mixing a fraction of Hartree-Fock exchange in GGA corrects the de-localization error, but this method is computationally expensive [195–197]. A computationally feasible and efficient way to treat this over-delocalization is the rotationally invariant DFT + Hubbard U method, which corrects the onsite Coulomb interactions and allows significant improvement over LDA and GGA [198]. We varied the empirical U parameter from 1-6 eV for the magnetic elements Mn and Ni to check the effect on the magnetic moments and electronic band gap. We found 4 eV for both the Mn and Ni was used throughout the calculations because increasing it further did not change the band gap in the system. We used the projected augmented wave (PAW) potentials with $4f$ states of Sm atoms in the semicore state, which results in the valence electron for Sm: $5s^2\ 6s^2\ 5p^6\ 5d^1$ and La: $5p^2\ 6s^2\ 5d^1$. We used the following valence electronic configurations for: Ni: $4s^1\ 3d^9$; Mn: $4s^1\ 3d^6$; and O: $2s^2\ 2p^4$, respectively. The 6 X 6 X 4 Monkhorst-Pack set of **k** points were used for the Brillouin zone integration for the unit cell of 20 atoms and scaled proportionally in supercell calculations for better energy comparisons [199]. We doubled the **k** points in the self-consistent calculations to produce the density of states (DOS) in respective magnetic configurations.

5.3 Results and discussion

5.3.1 Structural analysis

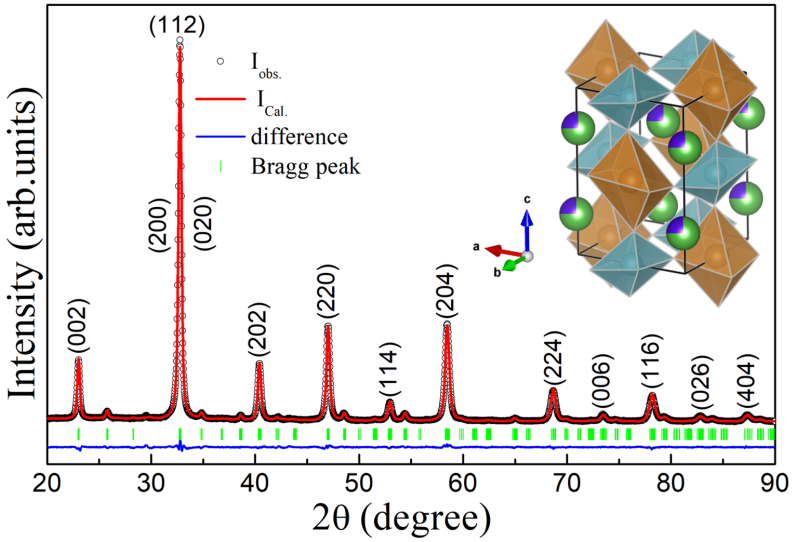

Fig. 5.1 Room-temperature XRD pattern of LSNMO where the black dot, red line, blue line, and green sticks represent the raw data, fitted data, difference, and Braggs position, respectively. Inset shows the polyhedral picture of the unit cell where the green/blue ball represents the La/Sm and light blue and brown octahedra denote NiO_6 and MnO_6.

The XRD pattern of LSNMO compound is recorded at room temperature to characterize the phase purity and other structural parameters. Figure (5.1) shows the XRD pattern and Rietveld refinement with FULLPROF SUITE for the 2θ range of 20 -100°. The crystal structure of LSNMO has been identified to exhibit monoclinic symmetry (space group: $P2_1/n$). The structural parameters are highlighted in Table (5.1). It is important to mark that parent compounds $LaMnO_3$, $LaNiO_3$, and $SmNiO_3$ crystal structure belong to orthorhombic (space group: Pnma), rhombohedral (space group: $R\bar{3}c$), and orthorhombic (space group: Pbnm) categories, respectively [144, 200, 201]. LSNMO compound transforms the crystal structure towards a lower symmetry, *i.e.*, monoclinic due to the substitution of La with Sm (or Ni with Mn) and induced octahedral distortions. The lattice parameter of the monoclinic system is 5.4651, 5.4626, and 7.7401 Å, and the angle (β) is equal to 89.7684°. The fitting parameters R_p, R_{wp}, R_e, and χ^2 are 5.60, 5.00, 3.26, and 2.35, respectively. Structural refinement also suggests that Ni-O (Mn-O) bond length and angle Ni-O-Mn $\neq$ 180° are distinct that consider as a microscopic mechanism of the orbital distortion in the crystal structure of the LSNMO. The values of Ni-O(Mn-O) bond-length and Mn (Ni)-O-(Mn) Ni bond-angle of LSNMO are distinct from an ordered LNMO [12, 26, 103].

Table 5.1 Room-temperature lattice parameter, bond length (Å), bond angle (°), and atomic position driven from Rietveld analysis of LSNMO XRD pattern.

Lattice Parameters (Monoclinic crystal structure $P2_1/n$ space group)							
a (Å)	b (Å)	c (Å)	α (°)	β (°)	γ (°)	V (Å^3)	χ^2
5.4650(1)	5.4625(6)	7.7400(1)	90	89.7683(4)	90	231.06	2.3
a (Å)	b (Å)	c (Å)	β (°)	Compound		Space group	Ref.
5.3638(5)	5.8517(5)	7.4825(5)	90	$SmMnO_3$		Pnma	[202]
5.4941 (4)	5.4941 (4)	13.3122 (2)	90	$LaMnO_3$		$R\bar{3}c$	[203]
5.525	5.484	7.767	90.02	La_2NiMnO_6		$P2_1/n$	[12]
5.35647(11)	5.52127(11)	7.61932(17)	90.030(26)	Sm_2NiMnO_6		$P2_1/n$	[204]
Bond length and bond angles							
La/Sm-O (Å)	Ni-O_1 (Å)	Ni-O_2 (Å)	Ni-O_3 (Å)	Mn-O_1 (Å)	Mn-O_2 (Å)	Mn-O_3 (Å)	
2.7165	1.9900	2.0504	1.5329	1.9680	1.8829	2.3430	
	Ni-O_1-Mn (°)		Ni-O_2-Mn (°)		Ni-O_3-Mn (°)		
	154.904		158.361		173.552		
Atomic position							
	x		y		z		
La/Sm (3+)	-0.0011		0.0250		0.2485		
Ni (2+)	0.5		0		0		
Mn (4+)	0		0.5		0		
O1 (2-)	0.2736		0.2768		0.0494		
O2 (2-)	0.2135		0.1914		0.5040		
O3 (2-)	0.4828		-0.0082		0.1973		

The degree of orbital distortion induces magnetic competition and geometrical frustration in disordered perovskite systems [12, 26, 61, 103, 142, 182].

Inset Fig. (5.1) depicts a restricted crystal structure of LSNMO. The Ni(Mn) cations are octahedrally coordinated by six oxygen atoms and constitute NiO_6 (blue), and MnO_6 (yellow) octahedra that are situated either at (1/2, 0, 0), (0, 1/2, 0) positions across the crystallographic directions. In the present study, the reported intensity of Ni(Mn) cationic ordering peak is weak and diminishes to the background noise level. The brightest peak is recorded at 33° corresponds to the (112) plane reflection [205]. This indicates that the corner shared NiO_6 and MnO_6 octahedra are not arranged alternately across the entire lattice uniformly which further originates the ASD in the LSNMO. However, the detailed characteristics of these structural ASD on magnetic characteristics will be further explored by employing various magnetization measurements in the following sections.

5.3.2 Valence state determination

A detailed exploration of local electronic structures of LSNMO elements like La *3d*, Sm *3d*, Ni *2p*, Mn *2p*, and O *1s* XPS measurements is presented. Figure (5.2(a)) shows the O *1s* XPS spectrum exhibit an intense peak across B.E. of 529.12 eV with an additional feature towards higher B.E.. The O *1s* spectrum is deconvoluted into distinct two peaks

with B.E. 529.10 and 531.27 eV indicating the coexistence of two different oxygen species in the LSNMO as reported previously in other compounds [206–208]. The oxygen peak at 529.10 eV is mainly assigned to the lattice oxygen (O^{2-}) (denoted as O_I) [206–208], while the other peak at 531.27 eV is controversial. The possible reasons can be attributed to weakly bound surface adsorbed oxygen species or other precursors [206, 208–210]. By considering number of O-*1s* XPS data of hydroxides and perovskites Dupin *et al.* proposed this O-1s peaks in the range of 531-532 eV [210]. These oxygen constituents represent the oxidation state of oxygen ions distinct from regular oxygen with a different co-valence of the Mn (Ni)-O bonds that reduce the surface of cations oxides. LSNMO crystallites were prepared by following a thermal treatment at 1050 K; therefore, the existence of the hydroxyl group at the top surface can be excluded.

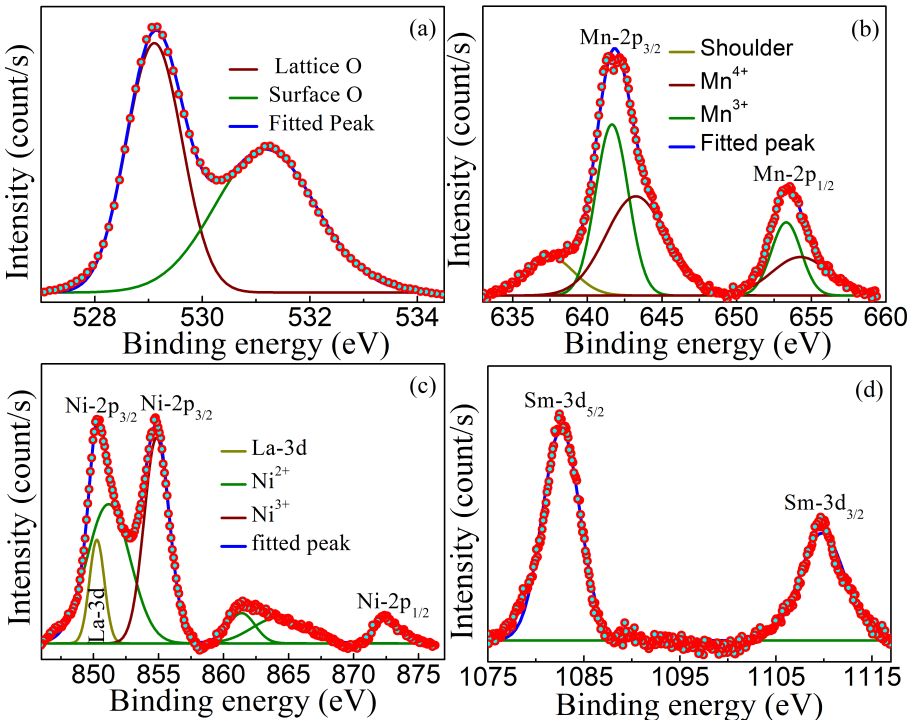

Fig. 5.2 XPS spectra of O *1s* (a), Mn *2p* (b), Ni *2p* (c), and Sm *3d* (d).

Fig. (5.2(b)) shows the Mn *2p* XPS spectrum consisting Mn $2p_{3/2}$ and Mn $2p_{1/2}$ doublet peaks due to the spin-orbit coupling that are peaked across 640.0 and 653.0 eV, respectively. The Mn $2p_{3/2}$ XPS peak can be deconvoluted into two fractions with B.E. at 641.65 and 643.24 eV, respectively, corresponding to the Mn^{3+} (Mn^{4+}) ions. In contrast, the Mn $2p_{1/2}$ XPS peak is also deconvoluted into two parts that are located having B.E. 653.31 and 654.26 eV, respectively, corresponding to the Mn^{3+} (Mn^{4+}) ions [211]. The molar fraction of Mn^{3+}/Mn^{4+} is estimated to be 0.954. Fig. (5.2(c)) illustrates the

Table 5.2 Room-temperature XPS analysis for sample LSNMO.

Parameter	Mn^{3+} $2p_{3/2}$	Mn^{4+} $2p_{3/2}$	Mn^{3+} $2p_{1/2}$	Mn^{4+} $2p_{1/2}$	Ni^{2+} $2p_{3/2}$	Ni^{3+} $2p_{3/2}$	Ni^{2+} $2p_{1/2}$
Peak position	641.65	643.24	653.31	654.26	851.15	854.85	872.54
FWHM	2.5842	4.7404	2.3503	4.5093	3.9268	2.2812	2.1712
Peak area	51669.92	54971.67	20093.94	20281.22	157306.14	135105.97	16247.37
Fraction	Mn^{3+}/Mn^{4+} = 0.954				Ni^{2+}/Ni^{3+} = 1.285		

combined La *3d* and Ni *2p* XPS spectrum that demonstrates a typical characteristic of the spin-orbit coupling and overlapping of both element's binding energies. The Ni *2p* XPS spectrum is split into two peaks at 851.3 and 855.3 eV, indicating the presence of La in 3+ oxidation state. Across 850 eV, the Ni $2p_{3/2}$ and La $3d_{3/2}$ peak overlaps with each other [211]. The Ni^{2+} $2p_{3/2}$ is located across 851.15 eV and Ni^{3+} $2p_{3/2}$ at 854.85 eV. However, Ni^{2+} $2p_{1/2}$ can be attributed to 872.54 eV. This observation indicates the existence of two different valence states of Ni ions, and the molar fractions of Ni^{2+}/Ni^{3+} are estimated to be 1.285. The above analysis of XPS indicates that there are two chemical states of Ni (Mn) ions in comparison to the ordered LNMO structure where the Mn (Ni) ions appear as 4+ and 2+ oxidation states [212], respectively. Sm $3d_{5/2}$ and Sm $3d_{3/2}$ at 1082.3 and 1109.2 eV with simulated lines shown in Fig. (5.2(d)). The deconvoluted spectrum shows the first peak located at 1082.3 eV attributed to the Sm-O-Sm bonds and the second peak at 1109.2 eV corresponds to the Sm-O-La ligands or any other oxide defects [53].

5.3.3 Temperature driven magnetic transitions

Measurements of M-T explore temperature-driven magnetic transitions and ground-state characteristics of LSNMO in zero-field-cooled (M_{ZFC}) and field-cooled (M_{FC}) under external magnetic fields (H_{dc}= 100, 500 Oe) as illustrated in Figure (5.3(a)). The major findings of M-T curve can be categorized in the following distinct types (i) the magnetization increases from 243 K in both the M_{ZFC} and M_{FC} curves, (ii) different rate of change for M_{ZFC} and M_{FC} across 243 K, and (iii) a bifurcation in the M_{ZFC} and M_{FC} magnetization across the irreversibility temperature T_{ir}= 243 K. All reported characteristics of M-T curves show resemblance with conventional magnetic frustrated systems such as canonical SG, cluster-glass (CG), and superparamagnetic (SPM) phase [39, 131, 183].

The presence of mixed valence state of $Ni^{2+/3+}$ and $Mn^{3+/4+}$ cations instigate multiple magnetic exchange interactions: (i) FM super-exchange interaction through $Ni^{2+}(e_g^2)$-O^{2-}-$Mn^{4+}(e_g^0)$ from of cationic ordering; (ii) $Ni^{2+}(e_g^2)$-O^{2-}-$Ni^{2+}(e_g^2)$ and $Mn^{4+}(t_{2g}^3)$-O^{2-}-$Mn^{4+}(t_{2g}^3)$ AFM interaction (iii) Ni^{3+}LS (e_g^0)-O^{2-}-Mn^{3+}HS (e_g^1) (LS: low-spin, HS: high-spin) cations driven FM interaction driven super-exchange; (iv) AFM super-exchange

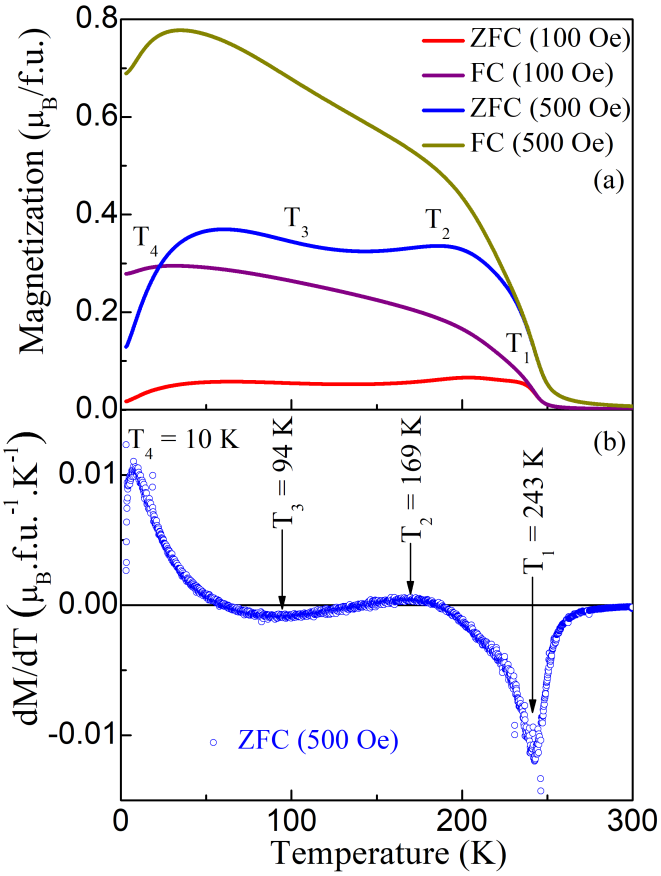

Fig. 5.3 (a) ZFC/FC magnetization curves recorded under an applied external magnetic field of 100 & 500 Oe, red colour represents ZFC, and purple colour represent FC, (b) dM/dT for dc magnetization in ZFC protocol at 500 Oe field value.

between pairs Ni^{3+} LS (e_g^1)-O^{2-}-Ni^{3+} LS (e_g^1) and Mn^{3+} HS (e_g^1)-O^{2-}-Mn^{3+} HS (e_g^1); (v) Ni^{2+}(e_g^2)-O^{2-}-Ni^{3+}(e_g^1) double-exchange interaction; (vi) Mn^{3+}(e_g^1)-O^{2-}-Mn^{4+} (e_g^0) ordering driven FM double exchange interaction [12, 26, 53, 103]. All these competing exchange interactions can modulate the local octahedral distortion as Mn^{3+} are Jahn-Teller active cations. LSNMO systems have dominating fraction of cation-ordered phase and mentioned interactions (i) and (iii). However, Ni^{3+} LS-O^{2-}-Mn^{3+} HS super-exchange interaction is less like to participate in the formation group state. These competing exchange interactions would lead to multiple magnetic anomalies [12, 26, 103]. The notable ordering temperatures of LSNMO compound can be observed from derivative of M_{ZFC}, *i.e.* (dM_{ZFC}/dT) as depicted in Figure (5.3(b)). Transition across 243 K is representing the PM $\rightarrow$ FM phase transition temperature (T_{c1}) that driven from the exchange interaction

between Ni^{2+}-O^{2-}-Mn^{4+}. The significant value of M_{ZFC} indicates a strong FM coupling between the Ni^{2+}/Ni^{3+} and Mn^{4+}/Mn^{3+} spins. Other prominent transitions are marked in Fig. (5.3(b)). The dominating AFM coupling is visible at lower temperatures in the ZFC curve.

Effective magnetic moment (μ_e^c) of LSNMO compound can be estimated using formula $\mu_e^c = \mu_B\sqrt{x(\mu_{Mn^{4+}})^2 + (1-x)(\mu_{Mn^{3+}})^2 + y(\mu_{Ni^{2+}})^2 + (1-y)(\mu_{Ni^{3+}})^2 + 0.5(\mu_{Sm^{3+}})^2}$, where $\mu_{Mn^{3+/4+}}$, $\mu_{Ni^{2+/3+}}$, and $\mu_{Sm^{3+}}$ is the magnetic moment for their respective HS Ni^{3+}($3d^7$, S = 3/2)/Ni^{2+}($3d^8$, S = 1) or Mn^{4+}($3d^3$, S = 3/2)/Mn^{3+}($3d^4$, S = 2), La^{3+} ($5d^0$) and Sm^{3+} ($4f^5$, J= 5/2), x and y are the phase fraction of Mn^{4+} and Ni^{2+}. For compound LSNMO, the values for x= 0.51 and y= 0.56, which is obtained from XPS study. The theoretical value for the magnetic moment for Sm can be calculated by equation $\mu = g\sqrt{J(J+1)}$. Considering g = 0.285 the obtained value for $\mu_{Sm^{3+}}$= 0.85 μ_B. The theoretical value for the magnetic moment for Mn(Ni) in their high spin states can be estimated by using the $\mu_{Mn(Ni)} = g\sqrt{S(S+1)}$. g = 2 for Mn and Ni cations give rise $\mu_{Mn^{4+}}$ = 3.87 μ_B, $\mu_{Mn^{3+}}$ = 4.90 μ_B, $\mu_{Ni^{3+}}$ = 3.87 μ_B, and $\mu_{Ni^{2+}}$ = 2.83 μ_B. For perfect ordered LSNMO compound the calculated μ_e^c = 5.55 μ_B. The difference between calculated and observed magnetic moments attributed to the prominent fraction of disorder sites in LSNMO [26, 36, 103, 183, 184]. The dominating nature of magnetic irreversibility in M_{ZFC} and M_{FC} near 243 K corresponds to an SG-like magnetic frustration that will be further explored in more detail in the following sections by manifestation of magnetic memory, training effects [143, 183]. The other three notable anomalies at T_2 (169 K), T_3 (94 K), and T_4 (10K) in M_{ZFC} can be visualized (see Fig. (5.3(b))) for LSNMO system. Across T_2 the AFM interaction is dominant because of antisites disorder that suppresses the magnetization. The wide transition across T_3 corresponds to phase separation representing the coexisting FM and SG phase [183]. Murthy *et al.* have observed that double perovskite $La_{2-x}Sr_xCoMnO_6$ (x = 0.1-0.5) displays antisite-disorder driven SG state [183]. The ZFC curve and large anisotropy between ZFC and FC curves at T_4 = 10 K suggest a frozen AFM transition that plays a major role in governing the EB effect in such magnetic frustrated system [183]. Eventually, LSNMO displays a PM $\rightarrow$ FM transition followed by a CG-like ordering at lower temperature [77, 185, 205, 213]. Additionally, two other new anomalies mainly reflecting the presence of antisite-disorder and competing exchange interactions in the system are observed. In contrast, the ordered parent LNMO displays a FM transition around T_{c1} $\sim$280 K due to the order spin state of Ni^{2+} and Mn^{4+} ions; however, for a disordered phase exhibits an additional FM transition around T_{c2} $\sim$150 K for the Ni^{3+}/Mn^{3+} magnetic phase with SG ordering across 38 K [12, 26, 53, 103].

5.3.4 Isothermal magnetization and critical analysis

Detailed exploration of magnetic transition and nature of involved exchange interactions in LSNMO compound are analyzed using scaling formalism of a set of exponents β, γ, and δ. Commonly, exponents β, and δ can be calculated from M_s and magnetic susceptibility χ_0(T) in proximity of T_c, while δ is the isothermal exponent. These critical exponents are correlated with M as expressed in following

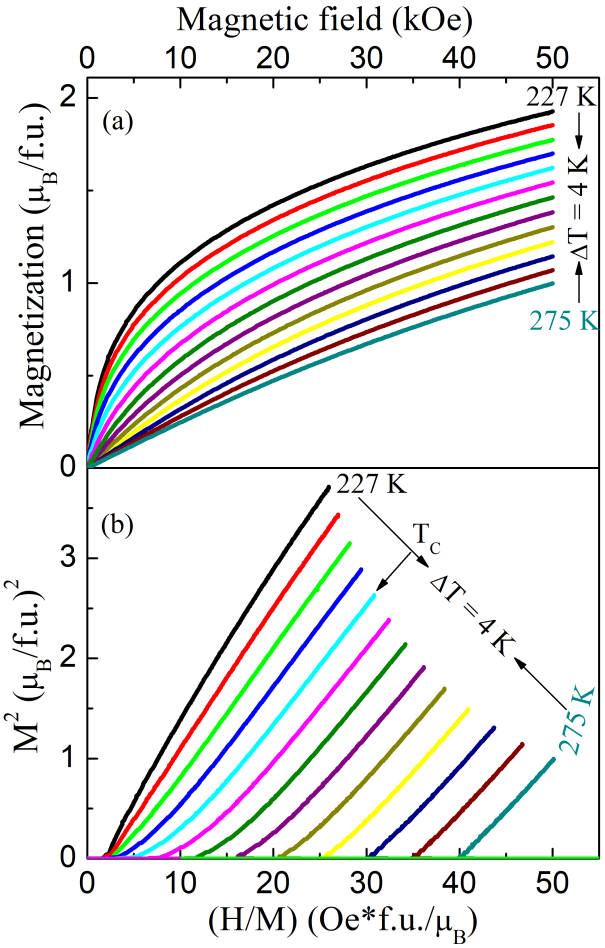

Fig. 5.4 (a) M *versus* H of LSNMO between 227 K and 275 K (in 4 K steps), (b) Arrott plots of M^2 vs (H/M) at different temperatures around T_c.

$$M_s(T) = M_0(-\varepsilon)^{\beta}; \qquad \varepsilon < 0, T < T_c \tag{5.1}$$

$$\chi_0(T)^{-1} = (h_0/M_0)\varepsilon^{\gamma}; \qquad \varepsilon > 0, T > T_c \tag{5.2}$$

$$M = DH^{1/\delta}; \qquad \varepsilon = 0, T = T_c \tag{5.3}$$

where ε = (T-T_c)/T_c reflects the reduced temperature, and M_0, h_0/M_0, and D are critical amplitudes. The β, γ, and δ are the critical exponents that are associated with M_s(T), $\chi_0(T)^{-1}$, and T_c [149, 158, 214]. The corresponding critical exponents can be collectively expressed as by equation $(H/M)^{1/\gamma}$ = (T - T_c)/T_c + $(M/M_1)^{1/\beta}$ where M_1 is a constant, the M_s(T) and $\chi_0(T)^{-1}$ are deduced from the high field region the modified Arrot plots (MAP). Fig. (5.4)(a, b) illustrates the isotherm M-H across 227-275 K and H/M *vs* M^2 plots. The positive slopes in H/M *vs* M^2 plots suggest that PM $\rightarrow$ FM as a second-order transition. The Arrott plots are non-linear where measurements were conducted to study the critical exponents using the mean-field theory model (β = 0.5 and γ = 1.0) [149, 158]. The mean field theory model across T_c, M^2 vs H/M at multiple temperatures display a series of parallel lines at T = T_c that insect through the origin [149, 158, 214]. The curves across T_c can be extended sharply into H/M axis to yield reliable values of the M_s (T,0) and $1/\chi_0$(T).

5.3.5 Isothermal magnetization loop

The gain the additional details of magnetic characteristics of the ground state we measure isothermal magnetization M-H loops up to $\pm$ 15 kOe across 5-300 K as depicted in Fig. (5.5). The right inset shows the pristine M-H curve from 0 $\rightarrow$ 50 kOe collected at 5 K indicating a well-saturated magnetization with H_c = 1.2 kOe. The M-H loop characteristics indicate the coexisting FM-AFM phases in the low-temperature region, excluding any SPM phases or blocking magnetic moments. At 300 K the M-H loop confirms the PM phase as evident by the straight line shape of M-H loop with negligible H_c and remanent magnetization (M_r) that also confirms the absence of any other magnetic impurity phases [50, 141]. Using the pristine M-H loop, theoretically the value of M_s can be estimated in the high-magnetic-field portion (H = 20-50 kOe) through using the relation M(H)= $M_s\left[1-\frac{a}{H}-\frac{b}{H^2}\right]$ + cH, where c is the high magnetic field differential susceptibility, a is nonmagnetic inclusion of local magnetic moments, and b reflects the magnetocrystalline anisotropy of the system [141]. The estimated value of M_s for LSNMO (right inset) is approximately 3.83 μ_B/f.u., whereas the M_s of a well-ordered LNMO should be 5.0 μ_B/f.u..

The temperature-dependent H_c of LSNMO compounds have been shown in the left inset of Fig. (5.5). The reduced value of M_s indicates the presence of a prominent fraction of antisite-disorders induced from mixed valence states of Ni (Ni^{2+}/Ni^{3+}) and Mn (Mn^{3+}/Mn^{4+}) that mainly caused through Sm^{3+} site-substitution for La^{3+}. The mismatch in the simulated to experimentally reported M_s values directly indicate the prominent presence of ASD [65, 103, 214, 215]. The influence of ASD on magnetic properties can be explained by substituting the Mn with Ni sites for an ordered LNMO where MnO_6

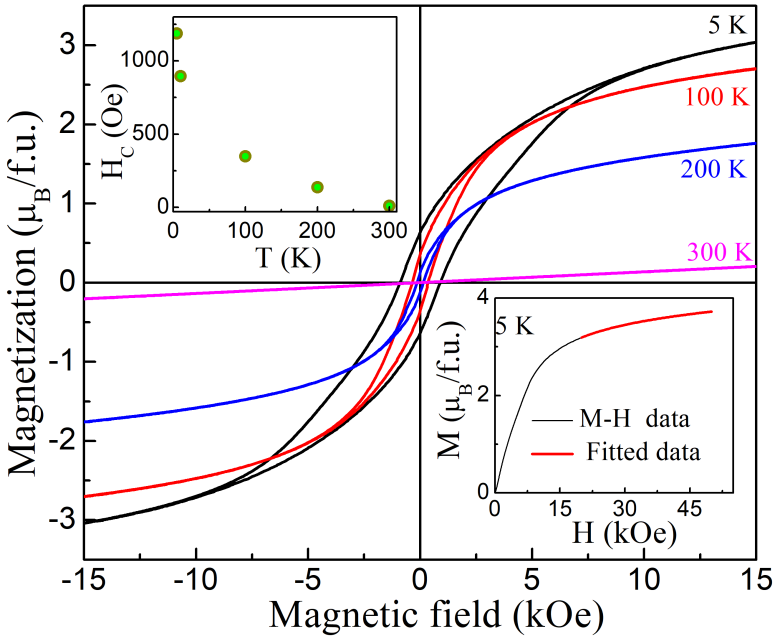

Fig. 5.5 ZFC isothermal magnetization at 5 K, 100 K, 200 K, and 300 K. Left inset shows the variation of the coercive field with temperature, and the right inset shows pristine M-H loops at 5 K up to +50 kOe.

and NiO_6 octahedra mutually periodically repeat themselves. In an ordered LNMO, each transition cation (Ni/Mn) is surrounded by six neighbouring transition metal ions Ni/Mn and displays FM correlation [141, 154]. For a disordered LSNMO, one Ni ion can be surrounded by five Mn and one Ni ions. A similar scenario is also considered for Mn ions. Therefore, such disordered LSNMO originated Mn^{3+}-Mn^{3+}, Mn^{3+}-Mn^{4+}, Mn^{4+}-Mn^{4+}, Ni^{2+}-Ni^{3+}, Ni^{2+}-Ni^{2+}, and Ni^{3+}-Ni^{3+} disorder pairs while every ordered site creates Ni^{2+}-Mn^{4+} and Ni^{3+}-Mn^{3+} pairs. The disordered pairs originate the AFM ordering whereas ordered ion pairs form the FM exchange interactions. Finally, these mutually competing interactions result from a magnetic moment in the presence of the prominent fraction of antisite disorders. The reduced magnetic moment is directly proportional to the degree of disorder present in the system [103].

5.3.6 Exchange bias and magnetic training effect

The presence of multiple short-range exchange interactions instigates magnetic frustration and anisotropic pinning centers across FM and AFM phase boundaries in the SG state. The exchange bias effect in the SG phase at pinning boundaries has been reported in earlier studies in likewise systems under field cooling conditions [77, 141, 143, 183]. These

findings motivate us to explore the magnetic frustration and competing FM and AFM interactions, spin-relaxation dynamics, and exchange bias effect across SG state of the LSNMO system. To monitor the EB effect M-H loops at 5 K in ZFC/FC conditions have been recorded with $H_{max} \leq \pm$ 15 kOe that allow excluding any minor loop effects (see Figure (5.6(a))). The M-H loop recorded in FC condition (H_{CF})= +500 Oe is shifted opposite towards the negative field direction in comparison to the M-H loop recorded in ZFC. The M-H hysteresis loop recorded with H_{CF} = -500 Oe is drifted in the reverse direction. The observation of a significant opposite shift for M-H loop $H_{CF} = \pm$ 500 Oe of the hysteresis loop is considered as a signature of robust EB effect in such a system. To monitor the EB variation with the H_{CF}, we recorded the M-H under the following protocol: cool down the system from PM state to 5 K under cooling field H_{CF} = 500 Oe and then recorded the M-H loops for the range $\pm$ 15 kOe. The measured M-H loops are found to be drifted along the negative field direction that terms as EB effect [171, 172]. It is also significant to mark that the LSNMO system does not display any shift in M-H loops recorded in ZFC condition. The M-H loops acquired with only FC condition observed to be shifted with magnitude $H_{EB} = (H_{c1} + H_{c2})/2$; where $H_{c1}(H_{c2})$ is ascending (descending) coercive fields [185, 205, 212, 213, 216, 217]. The observation of EB observed with multiple strength of H_{CF} as illustrated in Figure (5.6(b)). Inset shows the variation of EB on strength H_{CF} for 500 and 1000 Oe. Similar field-dependent variation of EB effect has also been reported for compounds $Sm_{1.5}Ca_{0.5}CoMnO_6$ [50], and $LaSrCoFeO_6$ [141]. The observed H_{EB} and corresponding H_c for H_{CF} = 500 Oe were $\sim$153 Oe and $\sim$ 1.2 kOe for the LSNMO compound.

The EB effects have been investigated extensively for magnetically frustrated systems, where the SG phase evolves from the competing FM and AFM exchange interactions [141, 171, 172]. For LSNMO crystallites, the pinning phase boundaries across FM and AFM phase interfaces are considered for robust EB effect. This magnetic frustrated ground phase is predicted in the various compounds such as $LaSrCoFeO_6$ [141], $La_{2-x}Sr_xCoMnO_6$ $LaSrCoFeO_6$ [183], and $LaFeO_3$ [218] perovskites that have reported the robust EB effect. During magnetic field cooling, the SG spins aligned along H_{CF} direction and within the range of $0 \leq H_{CF} \leq 10$ kOe the M_s of the FM state is relatively smaller and corresponding unidirectional anisotropy is larger which originate the H_{EB}. As a further increase of H_{CF}, the fraction of FM state and their volume steadily dominate the magnetic ground state. The major fraction of FM state reduces the contribution of unidirectional anisotropy in SG state across FM/AFM boundaries. Hence, the ground-state spin configuration of LSNMO compound is a collective state of three different competing magnetic phases, *i.e.*, spin-glass state, AFM ordering, and field-driven FM ordering.

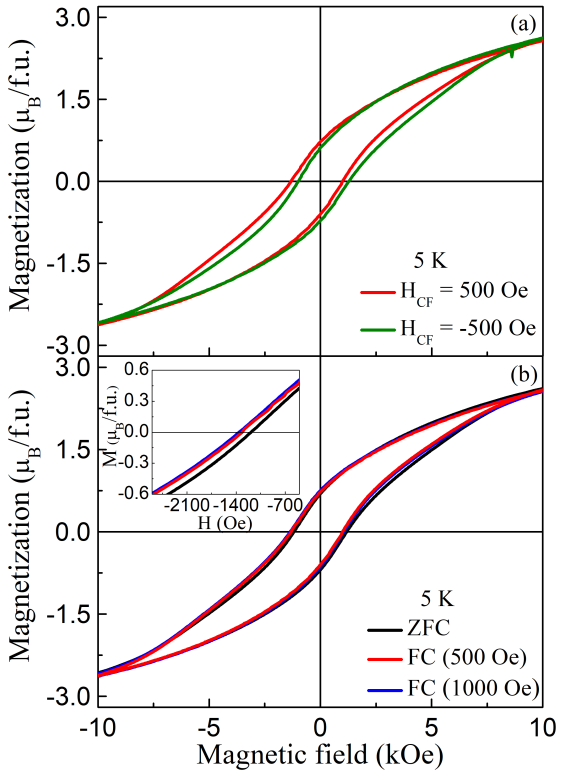

Fig. 5.6 (a) M-H measured at 5 K after cooling the sample from 300 K under a magnetic field of +500 Oe (black curve), and -500 Oe (red curve), representing the presence of exchange bias. (b) M-H loop measured at 5 K ZFC and FC mode in the presence of different cooling fields (0, 500, 1000 Oe). Inset shows the enlarged view.

The magnetic training effect that corresponds to a continues reduction of the H_{EB} with continuous magnetic field reversal is explored for magnetic inhomogeneous LSNMO compound. The training effect that is mainly characterized by a depression in strength of spin-torque impart by pinning boundaries in SG state of LSNMO. Depending on number of cycles (n), H_{EB} reduces sharply after the first cycle and continuously converges towards a threshold value in following cycles. Numerous empirical models have been proposed to describe the training effect and reduction of H_{EB} as a function n. It is widely accepted that during field cooling such frustrated compounds persist multiple FM clusters in an AFM matrix or vice-versa. The sharp reduction in H_{EB} and its variation with field cycles can described with n the framework of empirical power-law, *i.e.*, $\Delta H_{EB} \propto n^{-1/2}$ with $n > 1$. This model proposes during successive magnetic field reversal, large FM clusters transpire into a multidomain state, which is consistent with the Meiklejohn and Bean model that predicted a linear trend of H_{EB} for a FM/AFM system [219]. Magnetic training effect is a direct approach that provides the intrinsic EB effect in the form of spins rearrangement

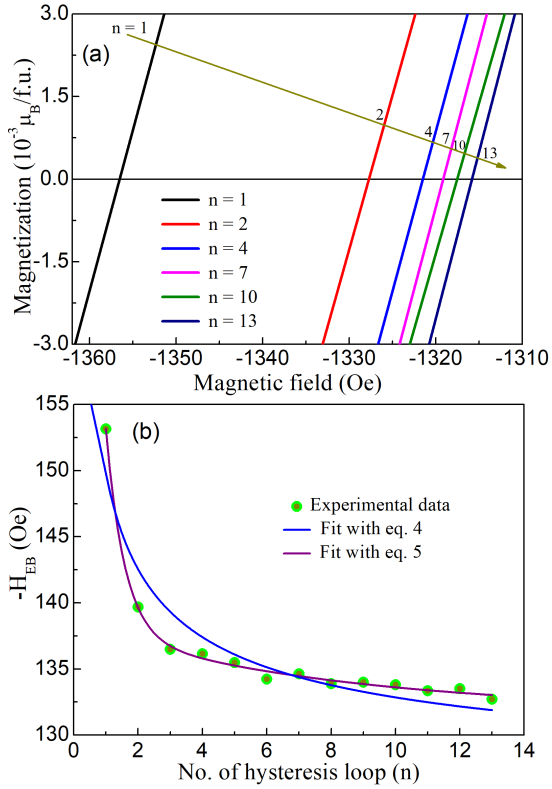

Fig. 5.7 (a) The zoomed view of hysteresis loop at 5 K after 1000 Oe cooling field with thirteen continuous cycles (magnetic training effect for EB). (b) The number of loops (n) dependent of H_{EB} extracted from training at 5 K. The blue solid line represents the best fit using empirical power law and the purple solid line represents the best fit as proposed by Mishra *et al.* 2009.

and their relaxation across pinning interfaces [217]. The spin rearrangement instigates a reduction in magnetic anisotropy and hence steadily lower H_{EB} as a function of n. We recorded total thirteen sequential M-H loops at 5 K with H_{CF} = +1000 Oe and the sweeping magnetic field range ± 15 kOe.

Figure (5.7(a)) highlights the M-H loops for the negative field quadrant for successive cycle numbers (n) of 1, 2, 4, 7, 10, and 13. Figure (5.7(b)) shows the training effect as confirm by non-monotonous reduction of $H_{EB}(n)$. Similar features of H_{EB} have also reported for other SG systems exhibiting the interfacial spin relaxation and modification of AFM spins pinning strength due to magnetization reversal [180, 219]. For LSNMO system, a significant change of H_{EB} ($\sim$ 67%) has noticed in between the $n = 1 \rightarrow n = 2$ cycles (shown in Fig. (5.7(b))). However, only 6% change in H_{EB} is noticed from n=2 $\rightarrow$ $n = 3$ cycles. This prominent reduction of H_{EB} suggests that across the pinning boundaries a finite fraction of pinned spins promptly reverse or flip with the external applied magnetic field [219]. Therefore, the frustrated spin state with dominating the pinning boundaries

driven instability of interface and H_{EB} as function n can be explained using following empirical law [217, 219, 220].

$$H_{EB}(n) - H_{EB}(\infty) \propto \frac{1}{\sqrt{n}} \tag{5.4}$$

where H_{EB} (∞) is the H_{EB} value for $n \to \infty$. The solid line (color online) in Fig. (5.7(b)) shows the best fit of H_{EB}, for n = 1 to n = 13. The best fitting parameters observed from numerical analysis using Eq. (5.4) is $H_{EB}(\infty)$ = 125 Oe.

The monotonous reduction of $H_{EB}(n)$ is mainly driven by relaxation of magnetic anisotropy across the pinning boundaries in the SG phase that significantly influenced by the rotating and frozen spins in the frustrated state. However, empirical power law approach only explains the dissipative energy of the AFM spins across the FM/AFM pinning boundaries. Therefore, it is difficult to capture entire details related the change of H_{EB} as a function of n using the empirical law expressed in Eq. (5.5). Recently, a suitable model proposed to describe the training effect, by considering both irreversible (frozen) and reversible spins for such magnetically inhomogeneous SG like phases [180]. The expression for this approach can be describe as

$$H_{EB}(n) - H_{EB}(\infty) = A_f exp\left(-\frac{n}{P_f}\right) + A_r exp\left(-\frac{n}{P_r}\right) \tag{5.5}$$

where A_f and P_f are the parameters associated to the modification of the frozen spins, A_r and P_r are parameters representing the reversible (rotatable) spin fractions of the frustrated spins across pinning boundaries of SG phases. It is significant to note that A_f and A_r have units identical to magnetic field, whereas, P_f and P_r are dimensionless parameters. From the fitting of H_{EB} data, the resulting parameters are H_{EB} (∞) = 131.8 $\pm$ 1.8 Oe (similar value obtained from empirical law), A_f = 87.68 $\pm$ 17.72 Oe, P_f = 0.57 $\pm$ 0.09, A_r = 6.53 $\pm$ 0.82 Oe, and P_r = 7.82 $\pm$ 6.17. The comparison of ratio between P_f and P_r suggests the modifications in the relaxation characteristics of both irreversible (frozen) and reversible (rotatable) spin fractions. In this study, we observe that the value of P_r is much higher than the P_f that indicates that the reversible spin relaxes approx. $\sim$ 14 times faster in compare to frozen spins across pinning FM/AFM boundaries in SG state. Recently identical magnetic training effect has reported in various other systems including $Sm_{1.5}Ca_{0.5}CoMnO_6$ [50] and $La_{2-x}Sr_xCoMnO_6$ compounds [141].

5.3.7 Spin-glass dynamics

Further exploration of the SG state and its characteristic relaxation dynamics frequency dependent (50-300 Hz) ac-susceptibility ($\chi^{'}$) monitor across the temperature 5-260 K. Figure (5.8(a)) shows the multiple cusps each representing the magnetic transitions are clearly visible in $\chi^{'}$. The inset of Fig. (5.8(a)) shows the frequency-dependent maxima of cusp at low temperature located in SG phase that show a continuous shift towards the higher temperature side as frequency increases. This shift induced through an extension of the action time mediated spin relaxation delay and observe shift is considered as an intrinsic signature of SG phase. Generally, Mydosh parameter, $\Omega = \frac{1}{T_f(\omega)} * \frac{\Delta T_f(\omega)}{\Delta ln\omega}$ is used to differentiate the various microscopic origin and mechanism of the spin relaxation and associated dynamics [39, 131]. The $\Delta T_f(\omega)$ represents the peak shift of such cusp as a function of frequencies. Typically for a magnetic frustration derived through cluster glass freezing, the value Ω yields range across 0.005–0.09, whereas for the frustration mediated through SPM phases Ω usually extended between 0.1-0.3. For LSNMO compound, the estimated $\Omega = 0.013$ indicates a dispersion in frequency dependent $\chi^{'}$ that mainly originates from the SG system [12, 39, 131]. This method is also used to exclude any feasibility of SPM phase [131].

The LSNMO system such as interacting spin clusters glass is best accounted for using the various empirical model to establish the link between the frequency (Ω) and the characteristic relaxation time (τ). The relaxation time τ associated to the peak temperature $T_f(\Omega)$ for every measured frequency $\Omega = 2\pi f$ was estimated utilizing expression $\tau = 1/2\pi f$ [12, 39, 131, 141]. The power-law behaviour which indicates critical slowing down has used to understand the relaxation mechanism [12, 141]. Apparently, the cluster SG systems and associated critical spin freezing dynamics can be also analysed through employing the VF formalism using the expression $\tau = \tau_0 * \exp\left(\frac{E_a}{k_B[T-T_{VF}]}\right)$, where, E_a is denotes the activation energy, k_B is Boltzmann constant, and T_{VF} is freezing temperature at which the spin dynamics manifest the dispersion and carries resemblance to the T_{SG} [12, 39, 131]. Commonly, the frustrated state through critical slowing down approaches the relaxation reflects a linear characteristic for $\ln(\tau)$ *vs* (1/T) plot [12, 39, 131]. While, VF formalism provides a good quality fit as appears from a line plot through the data points in Figure (5.8(b)). The observed simulated fitting parameters for VF law are $T_{VF} = (64.2 \pm 0.1)$ K, $E_a = 1.189$ meV, and $\tau_0 = 2.29 \times 10^{-5}$ s. It is important to mention that the value of activation energy is comparable to the activation energies reported for the other frustrated cluster SG systems [39, 131, 221].

The spin dynamics and associated dispersion across T_{SG} used to explore further details and model the frequency dependence of the SG freezing temperature $T_f(\Omega)$. The reported

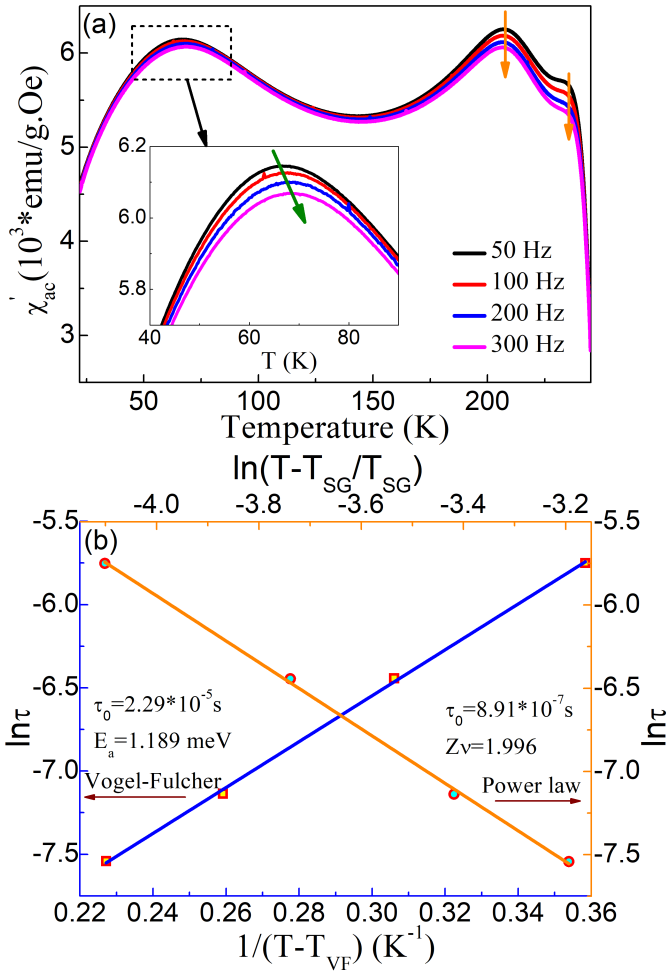

Fig. 5.8 (a) Real part of ac-susceptibility variation with the temperature at different frequencies 50, 100, 200, and 300 Hz. Inset show enlarge view of cusp shifting, (b) ln(τ) *versus* ln(T/T_{SG} - 1) and 1/(T - T_{VF}) plots for sample LSNMO, wherein the blue and orange solid line represents the best fit of Vogel-Fulcher and Power law, respectively.

dispersion at T_{SG} can be simulated using expression $\tau = \tau_0 \left(\frac{T_f(\omega)-T_{SG}}{T_{SG}}\right)^{-z\nu}$ with τ_0 is denote the characteristics of relaxation time, T_{SG} is spin glass transition temperature where τ displays the divergence, ν the critical exponent representing the correlation length $\xi = \left(\frac{T_f}{T_{SG}} - 1\right)^{-\nu}$ where z terms as dynamic exponent that can be expressed as $\tau \sim \xi^z$ [12, 39, 131]. The numerical analysis of ln(τ) with respect to $\ln\left(\frac{T_f}{T_{SG}} - 1\right)$ plot illustrated as a solid line in Figure (5.8(b)) provides T_{SG} = 65.9 K, $\tau_0 = 8.91 \times 10^{-7}$ s, and $z\nu$ = (1.996 $\pm$ 0.04). The reported higher value of τ_0 indicates a slow dynamic as predicted from a cluster SG system, where τ_0 is typically range $\sim 10^{-6}$-10^{-10} s. The higher values of τ_0 have been reported in various other systems like magnetite and perovskite nanoparticles

[39, 131, 158]. For archetypical SG system CuMn the value of τ_0 is in of order of $\sim 10^{-13}$ s that is significantly lower compare to the CG system [39, 131, 221]. Thus, both the power-law and VF approaches confirm the CG freezing with $T_{SG} \sim 65 \pm 1$ K.

5.3.8 Magnetic memory effect

The spin-relaxation process and magnetic memory effect displayed by these frustrated SG systems alternatively can also be explored by measuring the time-dependent magnetization M(t) [222]. Depending on the magnetic ground state a relaxation of frustrated spins toward equilibrium stable spin configuration leads a slow reduction of M(t) value [222]. Usually, CG system shows memory and rejuvenation effects due to degenerated ground state. To monitor the memory effect, first LSNMO sample field cooled from 300 K $\rightarrow$ 5 K under H_{CF} = 100 Oe, and a step followed by a warming thermal cycle to record M-T in presence of field was labeled FCW_{ref}. After approaching 300 K, sample follow a cooling cycle under the same field and record M-T, but briefly stop for a waiting time of 1 h at T = 50 and 25 K. During the waiting period magnetic field is set to zero and reapplied after then and cooling resumed [159, 160]. This magnetization measurement labeled as FCC_{stop}. After reaching low temperature (5 K) sample was again warming in the same field (100 Oe) and recording M-T without intermediate stops was labeled FCW_{memory}.

Figure (5.9(a)) manifesting the memory effect curve that exhibits step-like characteristics below T_{SG}. The step-like feature directly confirms the memory effect that is significantly prominent for the heating cycle curves where a step is completed. The manifestation of the memory effect also indicates the presence of an inhomogeneous SG system. This study presents the exclusive evidence of magnetic frustration in form of SG using multiple criteria. The relaxation time of SG state by thermo-remanent magnetization [159, 160]. The slow relaxation dynamics of thermo-remnant magnetization (TRM) below spin-glass transition in cluster spin-glass state has been a debated topic leading many theoretical and experimental investigations.

For strongly interacting SG systems, CG system, the M(t) should exhibit a stretched exponential behaviour which proposed by a generalized formula $M(t)=M_0 + M_r.\exp\left(-\frac{t}{\tau}\right)^{1-\alpha}$ where, M_0 is the characteristic magnetization component, M_r remanent magnetization of a glassy state, τ is the relaxation time, and α is the stretched exponent [159, 160]. For SG systems the numerical value of α mostly extends from 0 and 1. $\alpha = 0$ indicates mono-dispersive Debye-like relaxation dynamics and $\alpha = 1$ represents the lack of any relaxation. The mean range $0 < \alpha < 1$ indicates a non-Debye nature with relaxation times that emerges in the presence of many degenerate states in the magnetic frozen phase. Employing the generalized exponential function, in this section we understand the slow

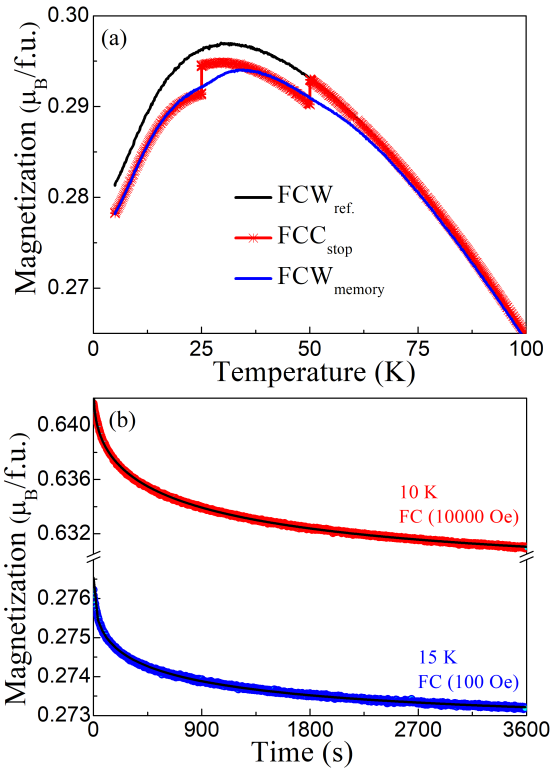

Fig. 5.9 Temperature-dependent FC magnetization data during memory measurement. (b) magnetic relaxation measurement at a different field and temperature and the black line represents the best fit using stretched exponent function.

relaxation of the glassy phase of LSNMO. To measure this, the sample was first cooled from 300 $\rightarrow$ 10 K under 10 kOe external magnetic field. Afterward, magnetic field has been removed and measures the magnetization decay. The results have shown in Figure (5.9(b)) where the continuous curve shows the excellent fitted to the stretched exponent formula with $M_0 = 0.273$ μ_B/f.u., $M_r = 0.004$ μ_B/f.u., $\tau = (566 \pm 6)$ s, and $\alpha = 0.603$ at 15 K and $M_0 = 0.629$ μ_B/f.u., $M_r = 0.014$ μ_B/f.u., $\tau = (832 \pm 7)$ s, and $\alpha = 0.546$ at 10 K. The values of the exponent α are in the span for spin-glasses and cluster spin glasses, which also suggests strongly poly-dispersive relaxation nature of the glassy systems.

5.3.9 Electronic structure

To give a firm footing to the interpretation of the magnetic properties of LSNMO, we have performed first-principles calculations to get quantitative insights into the microscopic origin of various magnetic interactions. The existence of ASD contributing to multiple AFM or FM transitions is also explored. We begin by investigating the ground-state

properties of the ordered LNMO with 25 % doping with an isoelectric Sm atom substituted at one of the La sites in the conventional unit cell of 20 atoms in the monoclinic phase. We relaxed the ionic positions at fixed experimental lattice constants described in Table (5.1). The relaxed atomic positions and bond lengths have slight variations from the experimental data in the FM state (see Table (5.1)).

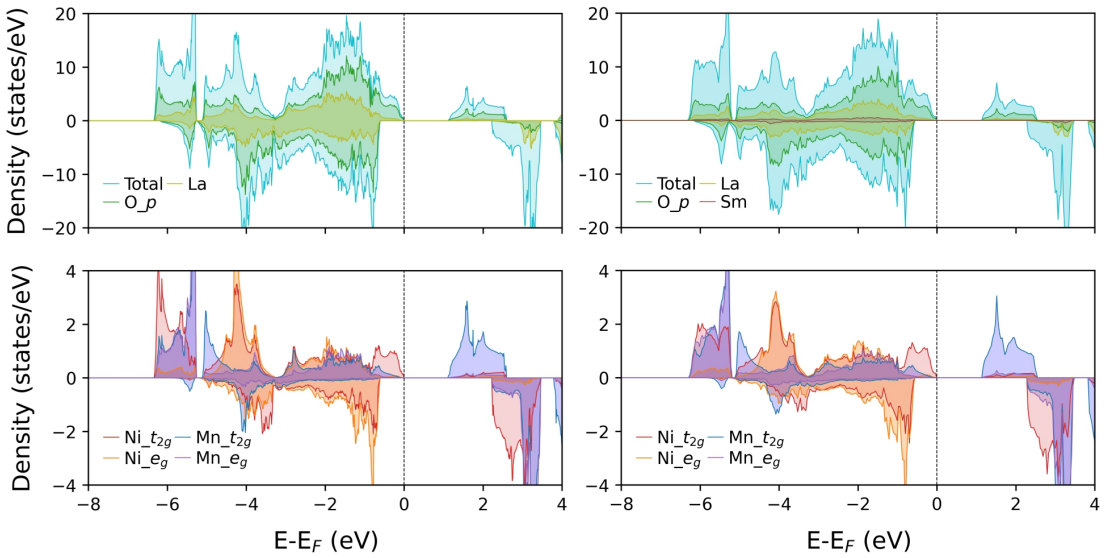

Fig. 5.10 Upper panel shows the spin-resolved total density of the pristine LNMO in the right column and LSNMO in the right column for the chemical ordered and ferromagnetic phase. It also shows the density projections on p-orbital of Oxygen atoms and La atoms in the right column; the left column also includes the contributions of the Sm atom. The bottom panels show the spin-polarized partial density of states for Ni_t_{2g}, Ni_e_g and Mn_t_{2g}, Mn_e_g respectively. The Fermi level in the DOS is set to 0 eV.

In FM configurations, each NiO_6 octahedra is tilted with respect to MnO_6 octahedra giving rise to the Ni-O-Mn bond angles vary between 154.3° to 159.37° depending on the position of the doped Sm atom. However, out of the plane, the Ni-O_3-Mn bond angle changes significantly with a variation of 153° to 159°, whereas experimental results suggested it to be 173.55°. This is due to the position of the O atom; in particular, the O_3 Oxygen atom differs noticeably from the experimental structure. This has already been reported in the literature [31, 59]. Experimental structures may have antiphase disorders in the system, and the possibility of oxygen defects can not be ignored either. This also gives a significant change in Ni-O_3 (2.03 Å) and Mn-O_3 (1.93 Å) bonds compared to the experimental values in Table (5.1).

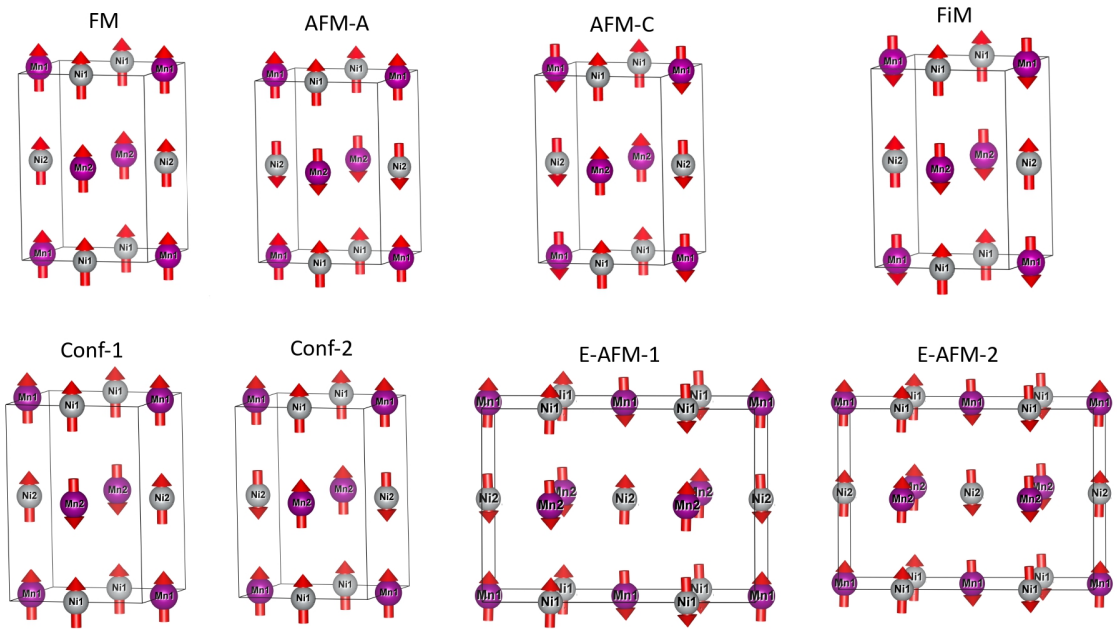

Fig. 5.11 Schematic representation of different magnetic configurations in LSNMO.

The ground-state magnetic configuration was determined by considering standard spin orientations on the Ni and Mn sites forming the FM, A-AFM, C-AFM, ferrimagnetic (FiM), and E-AFMs. Figure (5.11) also shows two configurations where two Ni and one Mn sites had a parallel spin, and the second Mn atom had an anti-parallel spin and *vice versa*. This implies the total magnetic moments in the system depend on whether Ni or Mn atom has an opposite spin. A description of these configurations can be found in Fig. (5.11). Our calculations suggest that the FM configuration is the most stable, as also observed in the experiment; the second most stable configuration is the AFM-A type (83 meV/f.u. higher), followed by AFM-C type (169 meV/f.u. higher) and FiM (246 meV/f.u. higher). The two configurations where only one element out of four magnetic elements has spin-down are also higher (120 meV/f.u.) in energy. However, this is not enough to explain the co-existence of various magnetic phases in the system and needs further investigation, which will be discussed in detail below.

Figure (5.10) shows the spin-polarized density of states (DOS) for the chemically ordered, lowest energy FM configuration for both the pristine LNMO and LSNMO. LNMO has an electronic gap of 1.13 eV in the majority spin channel and 2.83 eV in the minority spin channel, qualitatively matching with previous reports [31]. Doping with an isoelectric Sm^{3+} atom at one of the La^{3+} sites in the unit cell leads to small changes of the band gaps to 1.17 eV and 2.90 eV for the major and minor spin channel, respectively. The valence states mostly dominate the *p*-orbital contributions from the oxygen atom and *d*-orbitals

states of Mn(Ni) atoms. The octahedral environment of Mn and Ni atoms split the Mn-d and Ni-d manifolds into t_{2g}^3 and e_g^2 levels.

The site-projected, spin-polarised partial DOS shows that the valence states of Ni and Mn consist of ($t_{2g\uparrow}^3$, $t_{2g\downarrow}^3$, $e_{g\uparrow}^2$) and ($t_{2g\uparrow}^3$), where $\uparrow$ and $\downarrow$ signify the majority and minority spin states, respectively. The conduction band is formed by the $e_{g\uparrow}^2$ orbital of the Mn atom in the major spin channel and $t_{2g\downarrow}^3$, $e_{g\downarrow}^2$ of Mn atoms and $e_{g\downarrow}^2$ of Ni atoms in the minor spin channel. There is significant mixing of Mn-$t_{2g\uparrow}^3$ states and O-p states with Ni-$t_{2g\uparrow}^3$ and Ni-$e_{g\uparrow}^2$ bands in the major spin channel, whereas Ni-t_{2g}^3 bands are located in between dominant O-p states and the Fermi level. In the up-spin channel, the Mn-$t_{2g\uparrow}^3$ bands are filled and separated by a gap of $\sim$ 1.13 eV from the empty Mn-$e_{g\uparrow}^2$ levels. In the down-spin channel, both Mn-$t_{2g\downarrow}^3$ and Mn-$e_{g\downarrow}^2$ bands are located above the Fermi level in the energy range of $\sim$ 2.0 to 4.0 eV. This results in the oxidation state of Mn and Ni being Mn^{4+} and Ni^{2+}, respectively, which agrees with the previous results in the pristine system [31]. The calculated magnetic moment per formula unit in the FM configuration of LSNMO is 4.93 μ_B, which is close to previously reported experimental values for LNMO [26, 31, 103]. Spin moments of Ni and Mn are 1.59 μ_B and 3.29 μ_B; small magnetic moments are also associated with the oxygen atoms. The variation of magnetic moments is expected with varying U parameters; an increment in the U parameter tends the more localization that affects the magnetic moment. Both LNMO and LSNMO are insulators in FM ground states. The Ferromagnetism in these systems is expected to be dominated by the superexchange interaction of the half-filled d-orbital of one of the metal ions with the vacant d-orbital of another metal ion through p-orbital of the oxygen atom. The occupation of the Ni-d states and Mn-d states leads to the conclusion of FM superexchange in Ni^{2+}-O^{2-}-Mn^{4+} similar to the pristine LNMO.

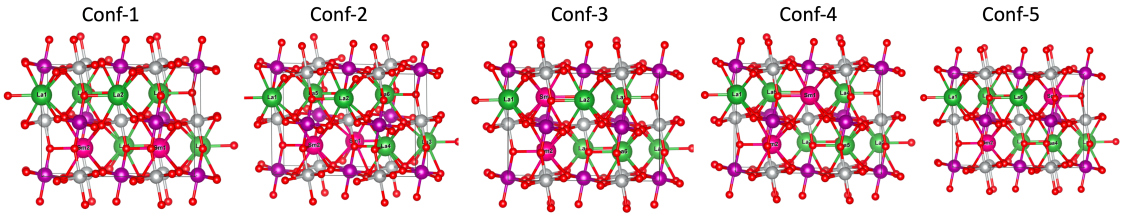

Fig. 5.12 Schematics of Sm substituted LNMO in 2 × 1 × 1 supercell. These configurations stand for the doping positions where 2 La atoms are replaced by the Sm atoms. The red colour balls stand for oxygen atoms; the silver colour shows the Ni atoms; the purple colour balls show Mn atoms. The light brown colour balls are La, and the pink colour shows the dopant Sm atoms.

Figure (5.12) shows the different doping configurations of the Sm atoms. We tried to vary the dopant positions in 2 × 1 × 1 supercell where two La atoms should be substituted by the Sm atom for 25 % doping. We checked if both the Sm atoms get to replace in

Table 5.3 Comparison of energies in FM configurations for 2 × 1 × 2 supercell with various doping arrangements described in Fig. 5.13.

Configurations	Energies (eV/f.u.)	Relative energies (meV)	Magnetic moment (μ_B/f.u.)
Conf. 1	-74.0739	0	4.92
Conf. 2	-74.0802	-6.38	4.92
Conf. 3	-74.0784	-4.5	4.92
Conf. 4	-74.0764	-2.5	4.92
Conf. 5	-74.0686	5.29	4.92

the one unit cell or if they can energetically fever any specific configurations. It is pretty evident from Table (5.3) that the energy difference between different doping configurations is only a few meV/f.u. This suggests that we can choose the stands doping where one La atom per unit cell is replaced by the Sm atom.

It has been well established that in LNMO, the SG behaviour arises from the antisite and antiphase disorder in the system during the growth process [26, 103]. In the experimental section, we also see similar behaviour for LSNMO, but the transition temperatures are different than to previously reported LNMO [26, 103]. To test this in the notion of chemical disorder in LSNMO, we also investigated the antisite disorders in the unit cell and supercells. In the unit cell, we can exchange the position of one Ni and Mn atom and put the system in a disordered phase. Mn octahedra corners are shared in this phase with two Mn and four Ni octahedra. Unlike the ordered phase, FiM (110 meV higher than FM) configurations in antisites phases have the second lowest energies after FM, whereas in the ordered phase, it was AFM-A. However, in the experiments, it is highly unlikely to have perfect antisite phases. Rather, some antisite phase boundaries will be combinations in powder samples. To mimic the experiment and understand the properties of LSNMO in the presence of chemical disorder, we used 2 × 1 × 2 supercells with eight f.u., which contains 80 atoms. One Ni-Mn combination is in the antisite phase, where Ni-Mn can exchange places mutually in nearest neighbors as described in Fig. (5.13(a)) (denoted as system A in the following) or in different sub-units in as shown in Fig. (5.13(b)) (system B). In both systems, four Mn and four Ni atoms will occupy their correct sites. The rest of the eight (Mn, Ni) octahedral sites are occupied by an equal number of Mn_{Ni} (Mn atoms occupying Ni) or Ni_{Mn} (Ni atom occupy Mn sites) antisites. Five corners of Mn octahedra are shared with Ni, and one corner is shared with Mn and *vice versa*. The average bond lengths in these antisites structures match better with experimental data compared to the ordered phase, indicating the presence of ASD in the samples.

To understand the coupling between the magnetic moments of Mn and Ni cations in the presence of the ASD, we studied the energetic stability of three different magnetic

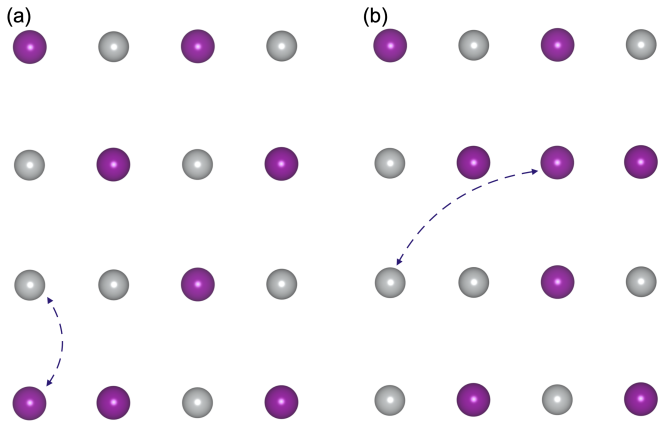

Fig. 5.13 Two-dimensional slice projection of 2 × 1 × 2 supercell of LSNMO shows the antisite defects ordering. In the left panel (system A), the Ni and Mn sites are exchanged cooperatively, and in the right panel (system B), Ni and Mn sites are exchanged in different unit-cell positions. In both of these systems, there are four Mn and four Ni atoms occupy their correct sites, and the rest of the eight octahedral; sites are occupied by an equal number of Mn_{Ni} (Mn atoms occupying Ni) or Ni_{Mn} (Ni atom occupy Mn sites) antisites results in 50 % of antisite mixing in the ordered phase. System A has a mutual exchange of Mn and Ni position in one sub-unit, whereas in system B, Ni and Mn atoms are exchanged from two different sub-unit in the supercell.

configurations for both the antisite structures in Fig. (5.8). We calculated three configurations: (1) FM phase in which all the spin directions are parallel both for Ni and Mn in the supercell (all the Mn and Ni ions have FM coupling); (2) FiM configuration, where all the Mn spins are antiparallel to the spins in the Ni atoms resulting in Mn ions having FM coupling with other Mn ions and AFM coupling with Ni ions and *vice-versa*; (3) Mn ions have AFM coupling with other Mn ions and FM coupling with Ni ions and *vice versa*, which results in three Ni and three Mn atoms in spin-up states and one Ni and one Mn atom in the supercell in the spin-down state. This last configuration is what we theoretically assume to have Ni^{2+}-O^{2-}-Mn^{4+} in FM exchange, Mn^{4+}-O^{2-}-Mn^{4+}, and Ni^{2+}-O^{2-}-Ni^{2+} in AFM exchange interactions. There is also a possibility for other magnetic interactions in these cases, but we stick with these three. These three configurations for two systems were relaxed for the ionic position at fixed experimental lattice constant.

Table (5.4) shows the relative energies in three different magnetic phases for two antisite systems described in Fig. (5.13). These disorders introduce some variations in the lengths of Mn-O and Ni-O bonds, respectively. These three configurations have a significant energy difference, clearly suggesting that conf. (3) is possible because they are only 20 meV and 40 meV higher than the FM phase in both antisite systematic models. In addition to this, conf. (1) has higher energies for both the systems as (0.20 eV higher for system A and 0.33 eV higher for system B) compared to FM configurations in ordered

Table 5.4 Comparison of energies in ASD phases in 2 × 1 × 2 supercell for various magnetic phases configuration 1, 2, and 3 as described in the text. The energies are compared independently for system A and system B.

		Energy (eV/f.u.)	Relative energies (eV/f.u.)	magnetic moment (μ_B/f.u.)
system A	Conf. 1	-73.769	0	4.94
	Conf. 2	-73.569	0.20	1.46
	Conf. 3	-73.741	0.02	3.71
system B	Conf. 1	-73.742	0.246	4.94
	Conf. 2	-73.552	0.189	1.45
	Conf. 3	-73.704	0.04	3.961

LSNMO. In addition to the stable energies, conf. (3) has a magnetic moment of 3.71 μ_B/f.u. and 3.96 μ_B/f.u. for system A and system B, respectively (see Table (5.4)). These match well with the observed saturation magnetization is 3.83 μ_B/f.u. in the inset of Figure (5.4). The other two configurations have a magnetic moment 4.94 μ_B/f.u., 1.46 μ_B/f.u. for system A and 4.94 μ_B/f.u., 1.45 μ_B/f.u. for system B, respectively. Therefore, this qualitative picture suggests that the magnetic transitions at lower temperatures are the response due to the ASD and APB in the sample.

5.4 Conclusion

In conclusion, we reported the synthesis of LSNMO crystallites in a monoclinic structure, the mixed valence states of Mn (Mn^{3+}/Mn^{4+}) and Ni (Ni^{2+}/Ni^{3+}) elements in the crystallites. The existence of mutually competing exchange interactions that occur through cations' mixed valence states is confirmed. The competing exchange interaction owing to the magnetic frustration originates various multiple magnetic transitions, and T_c are reported across 300 → 5 K. The multi-magnetic states are present in this ASD in LSNMO crystallites that also display low-temperature SG transition ($T_{SG} \sim 65 \pm 1$ K) due to the magnetic competition between short-range FM and AFM orderings. The pinning of the moments across the FM and AFM pinning boundaries in the ground state is considered for the EB effect with $H_{EB} \sim 153$ Oe and $H_c \sim 1.2$ kOe. First-principles calculations also confirm that the LSNMO is an insulator, and various magnetic phases are the results of ASD in the sample. ASD gives the mixed exchange coupling between Mn and Ni atoms which eventually results in a reduction of magnetic moment per formula unit. The observation of the EB effect and magnetization anomalies for LSNMO crystallites makes it a potential candidate for spintronics applications.